Available online at www.sciencedirect.com

ScienceDirect

journal homepage: www.elsevier.com/locate/he

Unveiling the mechanism of controllable CO_2 hydrogenation by group VIB metal single atom anchored on N-doped graphite: A density functional theory study

Jiajun Zhang [a], *Bin Yang* [a,**], *Kai Hong Luo* [a,b,*]

[a] *Center for Combustion Energy, Key Laboratory for Thermal Science and Power Engineering of Ministry of Education, International Joint Laboratory on Low Carbon Clean Energy Innovation, Tsinghua University, Beijing 100084, China*

[b] *Department of Mechanical Engineering, University College London, Torrington Place, London WC1E 7JE, UK*

HIGHLIGHTS

- VIB metal-based SACs are versatile in both CO_2 activation and hydrogenation.
- Selective hydrogenation of CO_2 over the SACs highly depends on H migration.
- H* charge has tight affinity to its migration capacity over catalytic active site.
- Valence electron occupancy of $Mo^{\delta+}$ is a descriptor for attaining surface H* with electroneutrality.

GRAPHICAL ABSTRACT

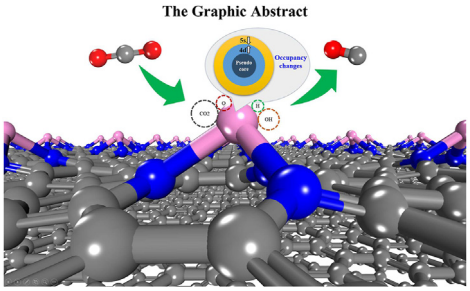

ARTICLE INFO

Article history:
Received 12 April 2022
Received in revised form
7 September 2022
Accepted 17 September 2022
Available online xxx

Keywords:
Decarbonization
Micro-environment of catalyst
Thermochemical conversion

ABSTRACT

CO_2 hydrogenation has raised considerable interest due to concerns about climate change. Realizing low-temperature reverse water gas shift (rWGS) reaction remains a significant challenge in the context of coupling it with the C–C growth reactions to convert CO_2 to C_{2+} fuels. We carried out systematic DFT simulations to unveil the underlying low-temperature mechanism for the selective hydrogenation of CO_2 to produce CO, over a variety of metal-based single atom catalysts (SACs) supported on the nitrogen-doped graphite. Group VIB metal-based SACs outperformed other 15 metal candidates in terms of versatile capacities in both selective activation of CO_2 molecule and facilitating escaping of CO and H_2O. Mo_1/N_3-Gt was especially outstanding by giving rise to spontaneous production of CO and O* through an effective electron injection into the CO_2 molecule. Water formation has been identified as the potential rate-controlling step in such a catalytic reaction over Mo_1/N_3-Gt with an energy barrier of 1.10 eV. Herein, the H migration played a pivotal role and had

* *Corresponding author*. Center for Combustion Energy, Key Laboratory for Thermal Science and Power Engineering of Ministry of Education, International Joint Laboratory on Low Carbon Clean Energy Innovation, Tsinghua University, Beijing 100084, China.
** *Corresponding author*.
E-mail addresses: byang@tsinghua.edu.cn (B. Yang), K.Luo@ucl.ac.uk (K.H. Luo).

https://doi.org/10.1016/j.ijhydene.2022.09.170

Please cite this article as: Zhang J et al., Unveiling the mechanism of controllable CO_2 hydrogenation by group VIB metal single atom anchored on N-doped graphite: A density functional theory study, International Journal of Hydrogen Energy, https://doi.org/10.1016/j.ijhydene.2022.09.170

Green hydrogen
Dynamic charge density

tight affinity to the charge of H* on the active site of catalyst. The dynamic coordination environment of $Mo^{\delta+}$ was revealed to be the dominant factor affecting the surface H* charge, leading to a variety of hydrogenation behaviors. The electron-deficient ligands of CO_2 and O* on Mo_1/N_3-Gt, as well as additional adsorbed H_2, were effective in adjusting the 4d and 5s electronic structure of central Mo and consequently resulted in nearly electric neutral surface H*s, thus most benefiting the hydrogenation process. The optimal charge of the coordinated Mo for an outstanding selective hydrogenation performance in this scenario was found to be no less than +1.7e.

Introduction

Decarbonization has achieved great progress globally in recently years, and energy saving and net-zero-emission (NZE) energy technologies are major contributors so far. Direct carbon capture and utilization (CCU), on the other hand, has not been widely applied yet [1], although it is crucial for closing up the carbon-neutral loop, especially for conventional energy and power industry, steel industry, and heavy or long-haul transportation, etc. [2]. With the rapid growth of the green hydrogen industry, CCU would potentially be able to overcome current economic hurdles and become extremely competitive through large-scale industrialization [3]. One can envisage that green fuels can be produced at scale using captured CO_2 in a traditional power plant by coupling CO_2 hydrogenation with Fischer-Tropsch synthesis (FTS) [4,5].

CO is a key fundamental compound for producing a variety of C_{2+} fuels. In an integrated bi-catalysts rWGS-FTS unit, the operational temperature for FTS reactions is normally below 400 °C while that for the standard rWGS reaction is normally higher than 500 °C because of its endothermic nature, leading to a remarkable operational temperature gap between the two reactions [6,7]. Realizing the low-temperature rWGS for coupling with the reactions of carbon chain growth remains a scientific question in such area. One should bear in mind that at a low temperature window around 300 °C, besides intrinsic activity of the catalyst, methanation is normally competing with the rWGS reaction. Therefore, catalysts are important to polarize the CO_2 molecule and facilitate the controllable hydrogenation to produce CO [8,9].

The reducible metal-based catalysts are most frequently applied in the rWGS reaction of CO_2 [10]. For example, Cu supported on metal oxides are efficient for CO_2 dissociation to CO [11,12], in which Cu^0 was oxidized by CO_2 to Cu^{1+} and reduced by H_2 [13,14]. However, metal clusters normally suffer from poor thermal stability because of facile aggregation. Catalysts of bimetal alloy catalysts and carbides-based catalysts are also exploited with boosted efficiency [15–18]. Wang et al. reported the Cu-in-Ni alloy catalysts, which attained nearly 100% CO selectivity in the full testing temperature range from 250 °C to 550 °C [19], benefiting from the facile decomposition of C═O and H_2 over the alloy active sites, as well as ready CO* desorption. Addition of noble metals has also been extensively investigated due to their good auxiliary catalytic effects in either promoting activation of reactants molecules or facilitating the CO desorption [20–22], but the high cost presents a barrier to their wide application. In this context, alternative base metal-based catalyst candidates are of increasing interest. Porosoff et al.[3,18] prepared a Co modified Mo_2C catalyst and found that one of oxygen atoms formed in CO_2 would quickly embed into the carbide surface to form Mo_2C–O, which would be reduced by hydrogen atoms dissociated from the Co surface, ensuring the stability of the intermediate CO* and promoting the rWGS reaction. The catalyst achieved a CO_2 conversion of 10% and a CO selectivity of 98% at 300 °C, outperforming noble metal alloys [23]. Lim et al. observed that $LaCo_{0.9}Ni_{0.1}O_3$ perovskite would realize the equilibrium conversion of CO_2 at 475 °C by a trade-off between H_2 dissociation efficiency and CO desorption over the CO–Ni alloy active sites [24]. In general, two mechanisms are widely accepted regarding the catalytic rWGS reaction of CO_2. CO_2 may experience direct dissociation to produce CO, and the surface oxygen is subsequently reduced by hydrogen, which is commonly known as the redox decomposition mechanism [25]. The other commonly reported mechanism is the intermediate decomposition mechanism, where CO_2 is firstly hydrogenated to formate [26,27], or carboxyl group [28], and then decomposes to CO and H_2O after further hydrogenation. An effective catalyst for the rWGS reaction should have moderate oxidable and reducible capacities with rich active sites, in order to attain both facile activations of CO_2 and H_2 and controllable H spillover and migration behaviors.

Single atom catalysts (SACs), normally coordinated in metal oxides, doped carbon or mimetic ligand chelate, are found to exhibit distinctive catalytic attributes towards CO_2 hydrogenation compared to ordinary solid catalyst, for instance metals oxides and transition metal carbides (TMCs) [29–31]. As a quasi-homogeneous catalyst, the SACs make the best use of the metal atoms and have good thermal stability given the anchored metal atom on 2D carbon materials. The micro-environment of the anchored metal atom is tunable according to its coordination and is also dynamic due to the attached ligands variation during reaction, giving rise to a variety of electron structures that may meet dedicated catalytic requirements. In recent years, the SACs catalysts have received increasing interest for a wide range of catalytic reactions, and there have been a number of endeavors looking at the SACs application in CO_2 hydrogenation [32,33].

Please cite this article as: Zhang J et al., Unveiling the mechanism of controllable CO_2 hydrogenation by group VIB metal single atom anchored on N-doped graphite: A density functional theory study, International Journal of Hydrogen Energy, https://doi.org/10.1016/j.ijhydene.2022.09.170

Most studies of SACs catalysts have been focusing on the formate products from CO_2 hydrogenation [34–36]. Other studies investigated the rWGS reaction over metal oxide supported SACs catalysts [37,38]. Millet et al. [39] indicated the Ni based SAC in MgO is highly active in the $2e^-$ redox cycle and gives rise to CO formation, because of the surface population modification by the Ni site, however the catalyst may still suffer agglomeration during reaction because of the surface carbonates decomposition, and Ni particles would give rise to the formation of CH_4 or MeOH. Another interesting metal oxides-based SAC is $Ir1/TiO_2$. Compared to Ir_5, the single-atom distributed Ir, resulting from the lattice matchiness of IrO_2 and TiO_2, led to great energy difference between CO dissociation and desorption during the CO_2 hydrogenation, such that it was also able to impede over-hydrogenation of CO_2 to CH_4 or formate products [40].

Carbon based SACs are increasingly appealing because they offer various coordination environments by elemental doping, and the carbon support is easily fabricated and has extensive resources [41,42]. Carbon (graphene/graphite)-based SACs have been widely used in the electrochemical and photo catalysis of CO_2 with carefully developed descriptors [43–45], and show great capacity in thermochemical catalysis [46]. Esrafili et al. [47] evaluated the thermal stability of graphene-based Co SAC by DFT modelling in detail, revealing the Co atom can be effectively stabilized in both three and four nitrogen coordination environments due to the strong hybridization of Co-3d and N-2p states. Sredojevic et al. applied DFT modelling to evaluate the performance of graphene anchored Ru and Cu SACs in terms of CO_2 hydrogenation, revealing the H atom hydrogenation pathway for Ru SAC and proton transfer mechanism for Cu SAC. They predicted the energy barriers were less than 0.87 kcal/mol during formic acid production. The study also concluded that Ru based catalysts had higher stability than Cu due to stronger metal-carbon binding [48]. However, another study found that a different coordination of C_2N would promote the Cu SAC effectiveness by lowering the highest energy barrier to 0.53eV [49]. In a more recent study, Pd supported on the mono-vacancy of graphene was found to outperform Ru in catalysis with even smaller peak energy barrier of 0.69 eV for formic acid formation [50]. Although a few endeavors have been made to investigate the thermochemical CO_2 hydrogenation over carbon-based SACs, they mostly focused on the formation reactions of formate products. Fundamental insights into the effects of dynamic micro-environment during the catalysis are far from being complete, for example the electron-level descriptors linked to the intrinsic activity of catalysts are still lacking.

In this work, we describe the performance of a variety of carbon supported SACs in CO_2 hydrogenation by systematical Density Functional Theory (DFT) modelling. Especially, the underlying mechanism for the outstanding catalytic activity of group VIB metals-based catalysts is revealed. The principles of electrons filling inside the coordinated central atom for a facile H_2 activation and directional hydrogenation are finally unveiled. The DFT predictions in this study shed lights on the mechanism of the selective hydrogenation of CO_2 over graphite-based SACs catalysts at electronic level and provide fundamental understanding and referable evidence to precise design of catalysts for the thermochemical conversion of CO_2.

Methodology

Calculation details

The first-principle density functional theory plus dispersion (DFT-D) calculations were implemented in the Vienna Ab-initio Simulation Package (VASP) with dispersion corrections by the D3 method of Grimme. The generalized gradient corrected approximation (GGA) [51] treated by the Perdew–Burke–Ernzerhof (PBE) exchange-correlation potential was used to calculate the exchange-correlation energy [52]. The PAW pseudopotential was employed as the scheme in the representation of reciprocal space for all the elements [53,54]. The plane-wave cut-off energy was set to 450 eV for all the calculations. The Brillouin zone was sampled using a $2 \times 2 \times 1$ and $4 \times 4 \times 1$ Monkhorst-Pack k-point with a smearing of 0.1 eV for respective geometry optimization and static electron structures calculation. Spin polarization has been considered, and the self-consistent field (SCF) tolerance was set to 10^{-4} eV/atom. All the modelling was performed with a convergence threshold of 0.03 eV/Å on maximum force. No symmetry constraint was used for any modelling. The computational method is believed to give high precision results, evidenced by the validation of lattice constant for the graphite lattice (primitive cell) in this study; the difference between the computational value (2.466 Å) and the reported experimental value (2.470 Å) is very tiny, as shown in Fig. S1 [55].

All the models were based on a three-layer P (4×4) supercell of three nitrogen doped graphite (100) facet, and the bottom layer was fixed. A 15 Å vacuum region was created above the top layer of the graphite facet. MedeA 3.1.0 was used for model establishment and pseudopotential assembling for the calculation. Geometry optimization was implemented to each model before energy was calculated. Energy of all the geometries was calculated at 0 K in the DFT investigation with corrections of zero point energy (ZPE) based on frequency analysis. Bader charge was calculated for atomic electron analysis. The adsorption energy E_{ad} was determined by Eq. (1), where $E_{catalyst}$, $E_{adsorbate}$ and $E_{adsorbate/catalyst}$ are the total energies of clean catalyst, free adsorbate molecule and catalyst with adsorbed molecule, respectively. The transition state (TS) was completely determined by the algorithm of climbing image nudged elastic band (CI-NEB) combing with the Dimer method. The energy barrier of a reaction ($E_{barrier}$) was determined by the difference between the energies of transition state and reactant, as shown in Eq. (2), where $E_{transition\ state}$ and $E_{reactant}$ are the total energies of the transition state and reactant of a reaction, respectively.

$$E_{ad} = E_{adsorbate/catalyst} - (E_{catalyst} + E_{adsorbate}) \quad \text{Eq.1}$$

$$E_{barrier} = E_{transition\ state} - E_{reactant} \quad \text{Eq.2}$$

The electron density difference (EDD) was determined by Eq. (3).

Please cite this article as: Zhang J et al., Unveiling the mechanism of controllable CO_2 hydrogenation by group VIB metal single atom anchored on N-doped graphite: A density functional theory study, International Journal of Hydrogen Energy, https://doi.org/10.1016/j.ijhydene.2022.09.170

$$\Delta\rho = \rho_{adsorbate@N\text{-}Gt} - (\rho_{adsorbate} + \rho_{CNT}) \quad \text{Eq.3}$$

where $\rho_{adsorbate@N\text{-}Gt}$ is the electron density of the whole adsorbate + adsorbent system, and $\rho_{adsorbate}$ and $\rho_{N\text{-}Gt}$ are the unperturbed electron densities of the adsorbate and the adsorbent structure, respectively.

The stability test of catalytic active sites

The stability of the catalyst unit was evaluated in a harsh reductive atmosphere at the reaction temperature of 1000 K, as shown in Fig. 1. The AIMD simulation was implemented within the canonical (NVT) ensemble in VASP 5.4.4, using the model established in this work. The profiles of energy and temperature are shown in Fig. 1 (a) and (b), respectively.

Results have shown that the single anchored metal (Mo) in a three-nitrogen coordination unit would keep steady at 1000 K even in a reductive environment, indicating the stability of the catalysts during reaction.

Results and discussion

The adsorption and activation of key molecules over SAC active sites

An effective catalyst for CO production should be versatile. It is expected to activate CO_2 efficiently, and would also avoid deep hydrogenation of CO to produce methane. Herein, we screened 18 metals through extensive adsorption evaluations, as shown in Fig. 2 (a). We found Ir_1/N_3-Gt led to the highest adsorption energy of 2.16 eV to CO_2, followed by W_1/N-Gt for 2.01 eV and Re_1/N-Gt for 1.65 eV, respectively, while Au_1/N_3-Gt, Rh_1/N_3-Gt, Mg_1/N_3-Gt, Cu_1/N_3-Gt and Mn_1/N_3-Gt exhibited weak binding to CO_2 molecule (red dots in Fig. 2). For the interaction of the catalysts with the ultimate product CO, the model predicts that most of IB, IIB and VIIIB metals give rise to exclusively stronger binding to CO compared to CO_2, wherein Ir_1/N_3-Gt and Au_1/N_3-Gt lead to the highest desorption energy of CO being over 3.00 eV. These metal-based catalysts would be helpful to formate formation, which requires further hydrogenation to carbon but may not be helpful for the rWGS reaction. Group VIB and VIIB metals-based catalysts mostly lead to moderate desorption of CO, and Mg_1/N_3-Gt, Ni_1/N_3-Gt, Cr_1/N_3-Gt and Fe_1/N_3-Gt have especially weaker interaction with CO with the adsorption energies around 1.00 eV, which would benefit the facile escape of CO from the catalytic active sites.

For these metal-based catalysts with weaker interaction with CO, their interactions with H_2O were additionally evaluated, which is the other important product molecule in the rWGS reaction (green dots in Fig. 2). The desorption profile indicates that Fe_1/N_3-Gt and Mg_1/N_3-Gt have the highest adsorption energy of H_2O for 1.15 eV and 1.11 eV, respectively, while Cr_1/N_3-Gt gives rise to moderate adsorption for 0.88eV, and other metal-based catalysts including Ni_1/N_3-Gt, Mo_1/N_3-Gt, Re_1/N_3-Gt and W_1/N_3-Gt were predicted to most benefit the facile desorption of H_2O molecule with the adsorption energies ranging between 0.39 eV and 0.59 eV. The ready escape of H_2O is also crucial for the rWGS reaction and catalysts stability.

Based on the above adsorption energy analyses of the reactants and products molecules, group VIB metals-based SACs are observed to be superior to other metal candidates in terms of simultaneous higher adsorption energy of CO_2 and lower desorption energy of CO and H_2O, therefore, they are deduced to have potentially better performance in the rWGS reaction.

Three group VIB metal-based SACs were further investigated in terms of their interactions with the CO_2 molecule in a variety of adsorption configurations (as shown in Fig. S2). The feasible chemisorption of CO_2 including chair and linear configurations over all the three catalysts are shown in Fig. 2 (b). Compared to free molecule of CO_2, of which the bond length of each C═O is 1.17 Å and molecule angle 180°, the length of one C═O bond has been stretched by over 10% and up to 16%, and the molecule angle is bent by above 24% for all the analyzed configurations, indicating the obvious polarization effect of Cr_1/N_3-Gt, Mo_1/N_3-Gt and W_1/N_3-Gt on adsorbed CO_2. Surprisingly, we found the dissociative adsorption of CO_2 over W_1/N_3-Gt in both two adsorption configurations resulted in the surface species of CO* and O* (Fig. 2 b), and this may give rise to a low energy barrier pathway for the CO production.

Due to the electron-deficiency of CO_2, the molecule polarization over metal site is primarily based on selective

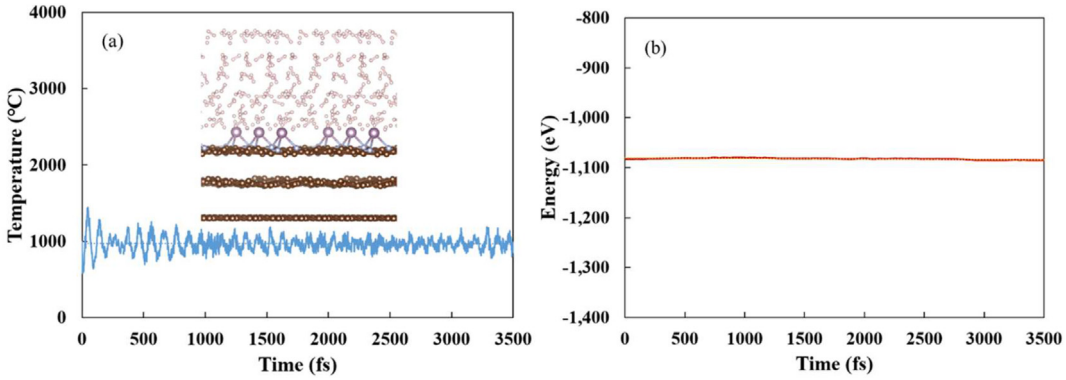

Fig. 1 – Temperature profile (a) and total energy profile (b) from AIMD simulation for Mo_1/N3Gt at 1000 k 3.5 ps (Brown denotes carbon, blue nitrogen, pink Mo and white hydrogen). (For interpretation of the references to colour in this figure legend, the reader is referred to the Web version of this article.)

Please cite this article as: Zhang J et al., Unveiling the mechanism of controllable CO_2 hydrogenation by group VIB metal single atom anchored on N-doped graphite: A density functional theory study, International Journal of Hydrogen Energy, https://doi.org/10.1016/j.ijhydene.2022.09.170

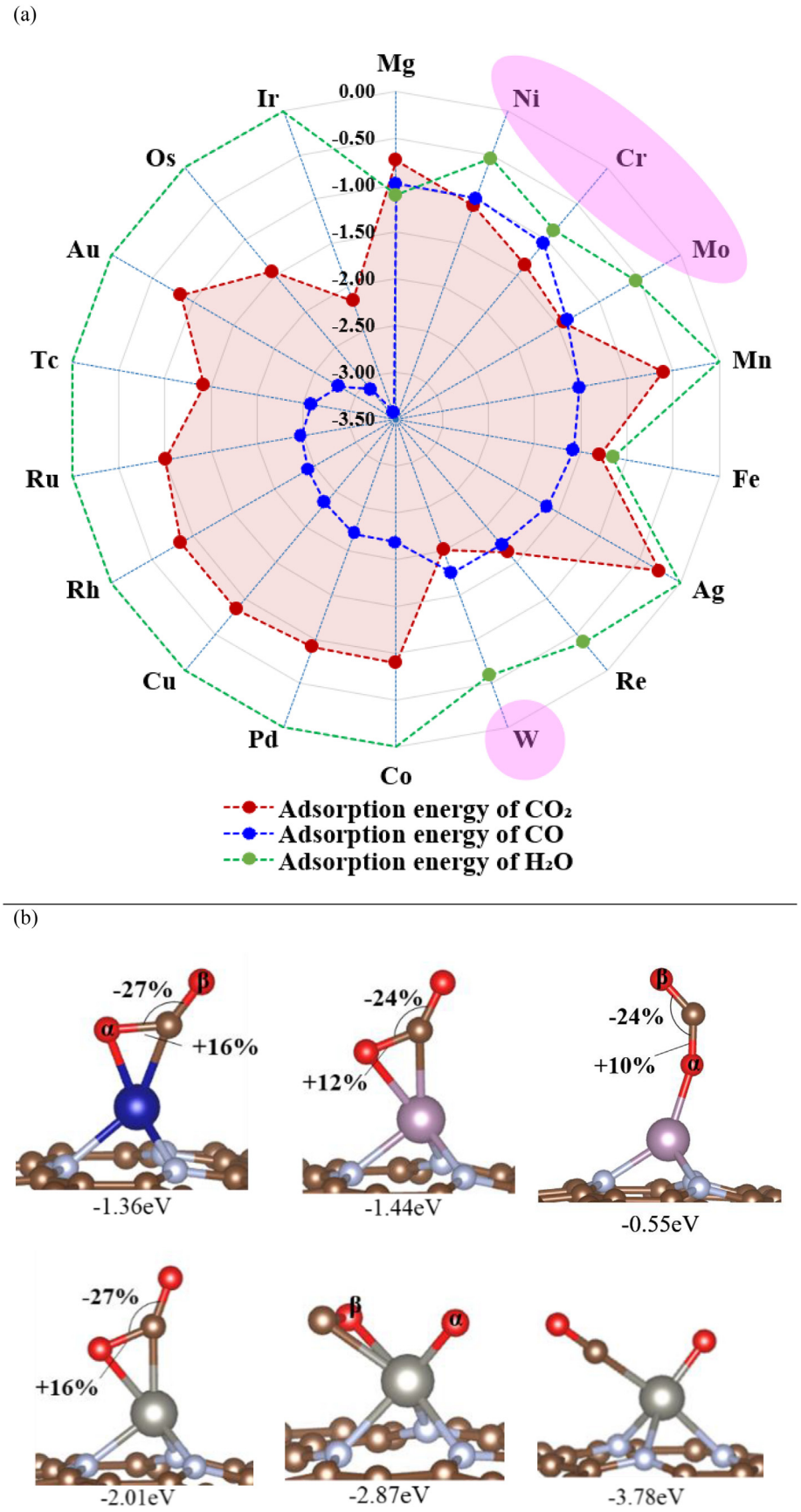

Fig. 2 – The adsorption energies (eV) of reactants and products over different coordinated metal active centers (a). Various CO_2 adsorption configurations over the group VIB metal-based catalysts (b).

Please cite this article as: Zhang J et al., Unveiling the mechanism of controllable CO_2 hydrogenation by group VIB metal single atom anchored on N-doped graphite: A density functional theory study, International Journal of Hydrogen Energy, https://doi.org/10.1016/j.ijhydene.2022.09.170

electrons injection. To further evaluate the activation of CO_2 by the anchored group VIB metal SACs, crystal orbital Hamilton population (COHP) analyses were adopted to analyze the bond strength, and the spin-discernible integrated values of COHP (ICOHP) were calculated to quantitatively describe the activation for respectively O_α-C and O_β-C, in comparison with free CO_2 molecule. We compared the group VIB metal-based SACs with Fe_1/N_3-Gt and Ni_1/N_3-Gt that also exhibited good interaction with the adsorbed CO_2 molecule. Fig. 3 (a) indicates the activation of O_α-C bond over Cr_1/N_3-Gt is more significant than that over Ni_1/N_3-Gt, evidenced by the apparent anti-bonding population at the Fermi level and more anti-bonding occupancy at deeper energy levels. The calculated results (Fig. 3 (b)) revealed that over group VIB metal-based catalysts, the averaged -ICOHP for O_α-C is around 6.2, which is much smaller than that in the intact CO_2 molecule, and is also smaller than that over Fe_1/N_3-Gt and Ni_1/N_3-Gt, indicating more electrons have been injected into the anti-bonding orbits of O_α-C bond by the group VIB metal based SACs, resulting in a better activation of the adsorbed CO_2 molecule.

The averaged ICOHP analysis results also show that the -ICOHP values for O_β-C bond over the above active sites are only slightly affected compared to the free molecule and are much bigger compared to that for O_α-C. This indicates the C_β-O bonds would remain stable throughout the adsorption in all scenarios, reflecting the potential superior product selectivity of the investigated SACs.

The behaviors of reactants activation over the nitrogen coordinated group VIB metal SACs were also compared with the single atom behavior of corresponding metal slabs (Fig. 4 and Figs. S3–S4). Other adsorption configurations of CO_2 and H_2 over top and hollow positions of the slab which bonded to multi-atoms are shown in Fig. S3.

The results reveal the bindings between the reactant molecules and one single metal atom in Mo (1 1 0) facet are weak. Only physical adsorption has been observed for both configurations of CO_2, with the adsorption energy of −0.16 eV and −0.13 eV, respectively. The adsorption of H_2 over Mo_1 in Mo (1 1 0) seems to be chemisorption but the activation is not prominent; the H–H length is 0.86 Å, close to 0.75 Å in a free H_2 molecule. Analogous results were also obtained for Cr (1 0 0) and W (1 1 0) as shown in Figs. S3–S4. The modelling of adsorption has revealed the distinct behavior of the nitrogen coordinated group VIB metal SACs in CO_2 activation through

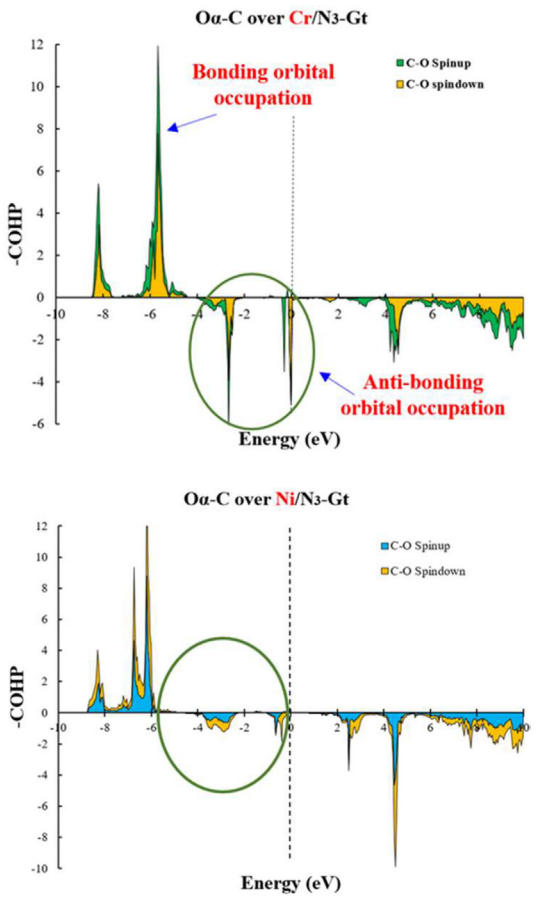

(a)

-ICOHP		Oα-C	Oβ-C	Oα-C	Oβ-C
CO_2	Spin-up	9.1890	9.1890	9.1890	9.1890
	Spin-down	9.1891	9.1891		
Over Cr	Spin-up	6.2477	8.5145	6.1532	8.5051
	Spin-down	6.0587	8.4957		
Over Mo	Spin-up	6.2571	7.4023	6.2556	7.4043
	Spin-down	6.2541	7.4062		
Over W	Spin-up	6.0920	7.4966	6.0893	7.4897
	Spin-down	6.0866	7.4828		
Over Fe	Spin-up	7.7820	8.7150	7.6903	8.6993
	Spin-down	7.5985	8.6837		
Over Ni	Spin-up	7.8804	8.9410	7.8302	8.8857
	Spin-down	7.7801	8.8305		

(b)

Fig. 3 – The COHP analyses of C–O bond in CO_2 over Cr_1/N_3-Gt and Ni_1/N_3-Gt (a) and integrated COHP over a variety of single metal based active centers (b).

Please cite this article as: Zhang J et al., Unveiling the mechanism of controllable CO_2 hydrogenation by group VIB metal single atom anchored on N-doped graphite: A density functional theory study, International Journal of Hydrogen Energy, https://doi.org/10.1016/j.ijhydene.2022.09.170

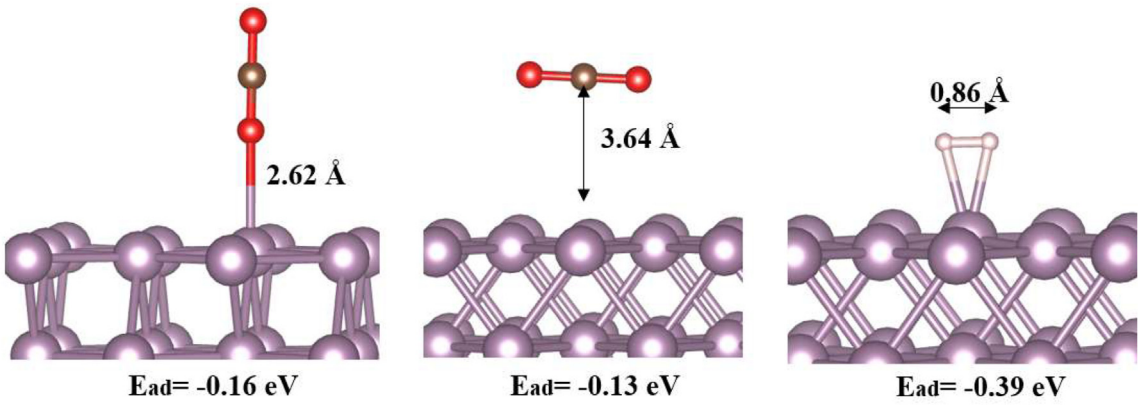

Fig. 4 – The activation of CO_2 and H_2 by one atom in Mo (110) facet.

selective electron injection, indicating their potential catalytic ability in rWGS reactions.

The catalytic pathways of CO_2 hydrogenation over group VIB metal-based SACs

The reaction pathways covering the full process of CO_2 hydrogenation over the group VIB metal-based SACs are shown in Fig. 5 (a) - (d), each elementary reaction consisting of structures of reactants, products and transition states. The energy barriers are highlighted, and the corresponding imaginary frequencies for all the transition states are listed in Table S1.

As shown in Fig. 5 (a), reaction starts from the dominant chair adsorption of CO_2 over Cr_1/N3-Gt, and the co-adsorbed H_2 is activated simultaneously. The activated CO_2* would experience direct dissociation when hydrogenation happens to O_α with an energy barrier of 0.43 eV, and produces CO*, and an *OH remaining on the active site along with H*. Alternatively, the hydrogenation may also take place on C with a smaller energy barrier of 0.09 eV, but the subsequent intermediate HCOO* is difficult to be further hydrogenated on Cr_1/

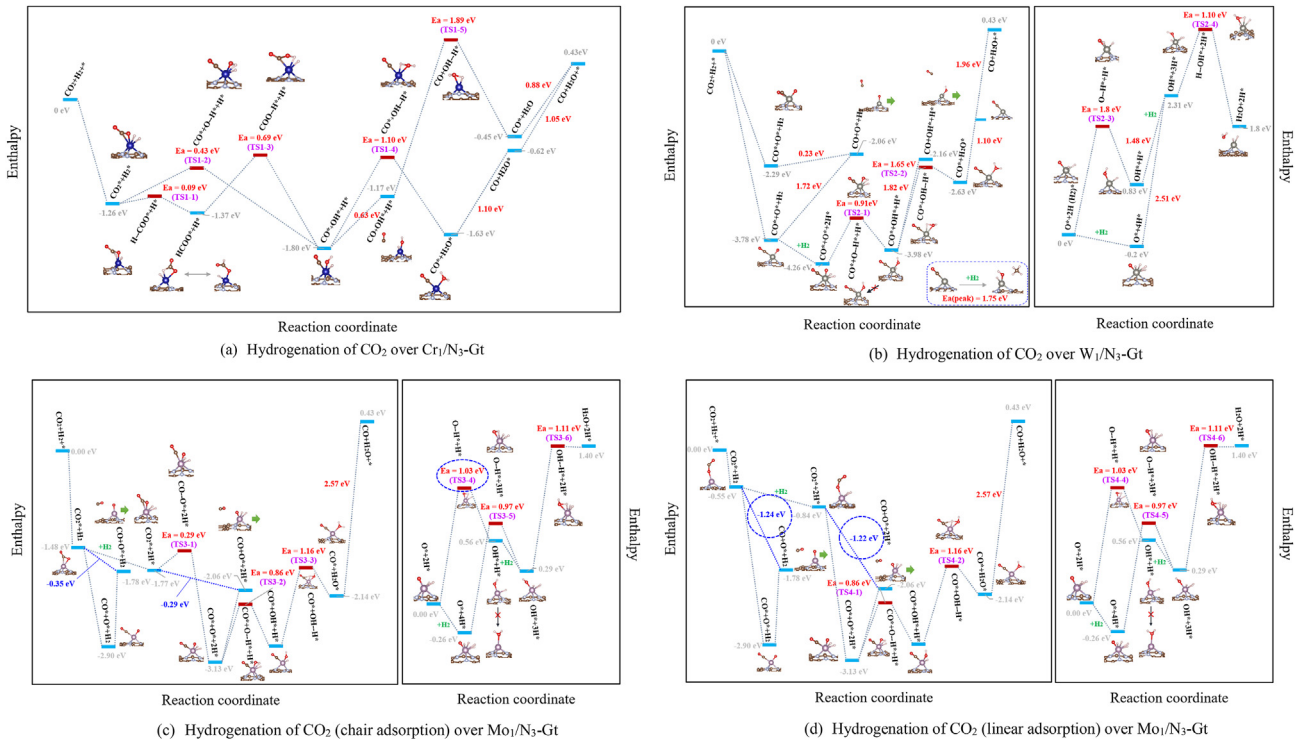

Fig. 5 – Reaction pathways (the red, blue, and grey respectively denote the endothermic process e.g., activation and desorption, exothermic process and relative enthalpy of one structure). (For interpretation of the references to colour in this figure legend, the reader is referred to the Web version of this article.)

Please cite this article as: Zhang J et al., Unveiling the mechanism of controllable CO_2 hydrogenation by group VIB metal single atom anchored on N-doped graphite: A density functional theory study, International Journal of Hydrogen Energy, https://doi.org/10.1016/j.ijhydene.2022.09.170

N3-Gt, and this has also been observed over Cu based active sites, on which such an intermediate would remain on the catalysts [56]. However, we find that the HCOO* intermediate would undergo alternative pathway by transforming to the *COOH intermediate, which further decomposes to CO* and *OH, with an energy barrier of 0.69 eV. The energy for CO_2 activation over Cr_1/N3-Gt is found to be lower than that over other 3d transition metal-based catalysts [57].

The modelling results reveal that the surface CO* would directly desorb rather than being hydrogenated, and the remaining *OH and H* species are the precursors for H_2O formation. The desorption of CO needs to overcome an energy barrier of 0.63 eV before the H_2O formation, while it surges to 1.10 eV in the presence of an adsorbed H_2O molecule. More importantly, we find the H_2O formation is supposed to be the potential rate-control step throughout the reaction, and its energy barrier highly depends on the micro-environment of the active site. The energy barrier for this step is 1.89 eV over clean active site (TS1-5), which is approximately 0.8 eV higher than that in the presence of adjacent CO* species (TS1-4). The underlying mechanism would be investigated in detail in Section 3.3.

In general, Cr_1/N3-Gt is predicted to lead to facile decomposition of CO_2 and H_2, as well as ready hydrogenation with quite small energy barriers, however, the H_2O formation by *OH and H* with an energy barrier of at least 1.10 eV seems to be a big hurdle for the rWGS reaction to take place.

Over the W_1/N_3-Gt, CO_2 is found to experience spontaneous dissociation after adsorption, resulting in two different dissociated configurations of CO* species, as aforementioned. One of the CO* species that has both C and O bonding to W_1 active site could desorb readily with an escaping energy of merely 0.23 eV, and the other adsorption configuration of CO* with a sole carbon bonding has quite large escaping energy of 1.72 eV (Fig. 5 (b)), resulting from the stronger binding of the end-on adsorption of CO. In the former scenario, the facile escaping of former CO* is more likely to leave a surface O*, which would experience subsequent hydrogenation with the co-adsorbed H_2. In the latter scenario, hydrogenation to O* would take place in the presence of CO* with an energy barrier of 0.91 eV, and the modelling also indicates CO* itself can hardly be hydrogenated on W_1/N_3-Gt, and the subsequent hydrogenation to *OH requires overcoming a large energy barrier of 1.65 eV, which is close to the escape energy of 1.82 eV for CO* on the catalyst. Following reactions involved in this pathway include the sequent desorption of CO and H_2O, with additional larger energy barriers up to 1.96 eV, and this would indeed kinetically impede the reactions in this pathway to happen. Due to the big escaping energy barrier of sole CO over W_1/N_3-Gt in this scenario, it could possibly be hydrogenated to produce methane after a transformation of its adsorption configuration, by overcoming a peak energy barrier of 1.75eV. The details are shown in Fig. S5.

For H_2O formation over W_1/N_3-Gt, as shown in Fig. 5 (b), the hydrogenation of O* species is found to have a similarly large energy barrier of 1.89 eV to that over Cr_1/N_3-Gt, besides, we found the subsequent hydrogenation to *OH is also difficult to take place with one surface H*, implying the H_2O is almost impossible to form over W_1/N_3-Gt. However, when an additional H_2 molecule adsorbed onto the active site adjacent to *OH + H*, we observed that the hydrogenation of *OH becomes feasible in such a system. This phenomenon is quite interesting which inspires us to carry out further investigation, as discussed in Section 3.3. It was also noticed that due to the special endothermic adsorption process of the additional H_2 in a *OH + H* system over W_1/N3-Gt, a big thermodynamic hurdle is posed for the hydrogenation of O* species in the presence of two co-adsorbed H_2 molecules, although the hydrogenation to *OH has an energy barrier of merely 1.10 eV.

The modelling results revealed W_1/N_3-Gt would lead to two different pathways for CO_2 hydrogenation, most likely undergoing the direct dissociation with a facile desorption of CO*, followed by the H_2O formation reaction with a peak energy barrier of 1.80 eV.

The hydrogenation of CO_2 over Mo_1/N_3-Gt exhibited a variety of pathways, resulting from the two different configurations of adsorption. Fig. 5 (c) shows the reactions starting from the chair-shape adsorption of CO_2, which experience direct decomposition which is different from that on W_1/N_3-Gt. We found two different pathways: CO_2* might decompose to CO* and O* followed by a CO desorption, having a deep well with strong exothermic and endothermic processes, alike the reported mechanism over Mo_2C [3]. The other pathway of decomposition takes place in a mild exothermic manner with a heat release of 0.35 eV and is accomplished with the spontaneous escaping of CO, which was rarely reported in the literature. For the co-adsorption scenario of CO_2 and H_2, a similar reaction scheme was observed, including the thermodynamic favorable reaction. The spontaneous CO escaping reaction was then confirmed by detailed structural evolution monitoring with five inserted points from the co-adsorption of CO_2 and H_2 and the end products, as shown in Fig. S6. The results revealed that all bond lengths are undergoing decreasing during the process except that the pre-cleaving C-O_β bond is getting stretched. The system enthalpy also monotonically declines, indicating the spontaneous release of CO from the active site is contributed by the reinforcement of all other bonds except the cleaving C-O_β in the surface species, and such reaction may give rise to O* and 2H* remaining on the active site. This reaction has also been validated at the reactive temperature of 500 °C through AIMD modelling, where the whole process for spontaneous production of CO was observed straightforwardly, as shown in Fig. S7.

In the deep-well reaction schemes shown in Fig. 5 (c), the decomposed CO* and O* are more likely to undergo sequent selective hydrogenation to produce CO* and H_2O*, with an energy-barriers of 0.86 eV and 1.16 eV. Regarding the hydrogenation of the lone O* over Mo_1/N_3-Gt, modelling reveals the *OH formation has an energy barrier of 1.03 eV, which is approximately 0.8 eV smaller than that over W_1/N_3-Gt, implying the superior catalytic effect of Mo_1/N_3-Gt. Nevertheless, the results also indicate the subsequent synthetic reaction by *OH and H* is rather difficult to take place, which we have observed in the scenario over W_1/N_3-Gt. However, with the presence of additional H_2 adsorption on Mo_1/N_3-Gt, the hydrogenation to *OH becomes feasible with an energy barrier of 1.11 eV. This result is in qualitative agreement with the observation over the active site of Mo_2C, where higher H coverage gives rise to more facile hydrogenation during H_2O formation [58], but interestingly, not

Please cite this article as: Zhang J et al., Unveiling the mechanism of controllable CO_2 hydrogenation by group VIB metal single atom anchored on N-doped graphite: A density functional theory study, International Journal of Hydrogen Energy, https://doi.org/10.1016/j.ijhydene.2022.09.170

a big difference of the energy barrier was observed for the hydrogenation to O* in both two scenarios of our study.

CO_2 hydrogenation starting from the linear adsorption configuration has analogous reaction pathways, but the spontaneous CO releasing step has much larger heat release of 1.24 eV and 1.22 eV, respectively in the presence and absence of H_2, thanks to the smaller adsorption energy for the linear adsorption of CO_2 over Mo_1/N_3-Gt compared to chair adsorption. Such severe exothermic reactions would benefit CO_2 decomposition and simultaneous production of CO.

The CO production from CO_2 hydrogenation is most favorable over Mo_1/N_3-Gt among the group VIB metal-based catalyst candidates. Especially for the potential rate-control step, H_2O formation with the peak energy barrier of 1.11 eV over Mo_1/N_3-Gt is found to be much more facile compared to that over W_1/N_3-Gt. In this regard, the overall performance of Mo_1/N_3-Gt to rWGS reaction is even superior to noble metal-based catalysts [59]. More importantly, the modelling also revealed that the kinetic hurdle of the selective hydrogenation reactions for H_2O formation was significantly affected by the dynamic coordination of the central metal atom, and the underlying mechanism is to be discussed in detail in the next section.

Dynamic electron structures of the active site for controllable hydrogenation of CO_2

The reaction modelling results indicate Mo_1/N_3-Gt outperforms Cr_1/N_3-Gt and W_1/N_3-Gt as a superior catalyst candidate for facilitating the rWGS reaction, while the most difficult step involved in the reactions has been identified to be H_2O formation, which is difficult to take place by sole H* and *OH on the active site. However, with additional H coverage on the active site, the H_2O formation becomes feasible. It was speculated that the migration capacity of the precursor species is crucial to H_2O formation [60], therefore, the bond strengths of both H*-Mo and *OH–Mo on Mo_1/N_3-Gt site were firstly evaluated in two different scenarios with altered number of additional H coordination, as shown in entry 3 in Fig. 6 (a) and Fig. S8. Based on the analyses of the variations of binding energy and COHP, we found only small differences were induced to the bond strength of H*-Mo and *OH–Mo after the coordination changed by the addition H attachments; for example, the binding energy for *OH–Mo with sole H* coverage is 5.13 eV and that for *OH–Mo with 3 × H* is 4.96 eV. For the H*-Mo bond, the binding energy also sees little variation with the addition of H adsorption. Moreover, the COHP analysis confirms that although the electron structures between these bonds have some changes during the coordination variations, the ICOHP values for both *OH–Mo and H*-Mo remain limited affected, as shown in Fig. S8 and Fig. 6 (b) and (c), implying the additional H_2 adsorption would not significantly alter the strength of *OH-metal bond or H-metal bond. This is also agreed by the similar analyses implemented for the H*-Mo and O*-Mo bonds in the co-adsorption scenario of H* and O*, as shown in the entry 2 in Fig. 6 (a). It was thus concluded that the facile H_2O formation induced by the additional H_2 adsorption may not result from bond strength variation of the precursor species in these scenarios.

Therefore, additional evaluation regarding electron structures of the migrating H* was implemented to reveal the underlying mechanisms for the different hydrogenation behaviors. Bader charges were then calculated for the two central Mo atoms in entry 3 of Fig. 6 (a), and surprisingly we found the H*s are carrying different charges on the same active site, and the charge highly depends on the number of adsorbed H* atoms; when there is only one H* and *OH co-adsorbed on Mo_1/N_3-Gt, the H* carries −0.34e, while when there are three dissociated H*s adsorbed, two of them are carrying −0.09e and −0.03e, nearly electric neutral, and another H* is still negatively charged and carries −0.29e. We suspect the variation of the H* charge is directly related to their migration behavior, and we analyzed the H* charges in other coordination scenarios of the co-adsorption of CO_2 and H_2, and the co-adsorption of O* and H_2, which are the key species in the reaction of H_2O formation. In addition, the charges of sole H_2 adsorption over Mo (1 1 0) and Mo_1/N_3-Gt were also evaluated for comparison, as shown in entry 1 in Fig. 6 (a). We found over the Mo (1 1 0) facet, the dissociated H*s are much negatively charged with −0.42e, while over the Mo_1/N_3-Gt, the H*s carry less negative charge (−0.36/-0.25). This may be due to the electronegativity of nitrogen coordination, evidenced by the charge density and electron density difference analyses shown in Fig. S9. Compared to sole H adsorption, the H*s are found to be close to electron neural with the coordination of CO_2*, carrying negative charges less than −0.06e in all the cases. With the coordination of O*, the analogous nearly electric-neutral H*s are observed, independent of the coordination number of H*s, as shown in entry 2 of Fig. 6 (a), and this may give rise to facile H migration and the subsequent electrophilic attack to O* to produce *OH.

A hypothetical electrophilic attack test was carried out to further justify the above mechanism, as shown in Fig. 7, where the hydrogen molecule has been completely dissociated and anchored on the Mo (1 1 0) facet, and a hydroxy group was placed adjacent to one of the hydrogens. We found that when the negatively charged H* getting close to the hydroxyl, the species are repulsing each other, and cannot react to form H_2O*. The *OH has even larger displacement than H* that is coordinated in the hollow by three Mo atoms. The results further confirm that the negative charge of H* is the key factor to impact H_2O formation and would be detrimental to the hydrogenation of O*. Such a conclusion was ultimately evidenced by a comparison with the co-adsorption of H* and O* over W_1/N_3-Gt, as shown in Fig. S10; the H* was much more negative charged by −0.28e, thus giving rise to a high action energy of 1.80 eV for the *OH formation, the precursor species for the H_2O formation. Only 1.03 eV for the same reaction was observed over Mo_1/N_3-Gt. The results indicate that the electric-neutral H*s would facilitate H_2O formation over Mo_1/N_3-Gt, and they benefit from the coordination of electron deficient groups.

Additional investigation was carried out to reveal the intrinsic connection between the induced H* charges and the dynamic coordination environment of the active site. The partial density of states (pDOS) of the central $Mo^{\delta+}$ in a dynamic coordination environment were calculated and shown in Fig. 8, in which the ratio for the occupied states was determined to exhibit the electron occupancy status, where the valence electrons in the 5s and 4d orbits of Mo are considered in the calculation. Fig. 8 (a) shows the occupancy of the

Please cite this article as: Zhang J et al., Unveiling the mechanism of controllable CO_2 hydrogenation by group VIB metal single atom anchored on N-doped graphite: A density functional theory study, International Journal of Hydrogen Energy, https://doi.org/10.1016/j.ijhydene.2022.09.170

(a)			
Structure entry 1	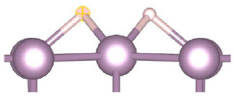 H_2 over Mo(1 1 0)	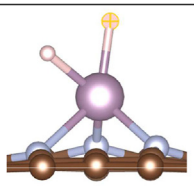 H_2@Mo/N_3-Gt	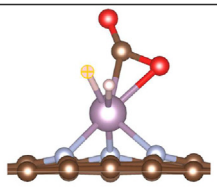 H_2-CO_2@Mo/N_3Gt
Binding Energy	-2.68 eV	-2.73 (-2.15) eV	-2.82 eV
Electron (involved)	1.42/1.41	1.36/1.25	1.06/1.04
Structure entry 2	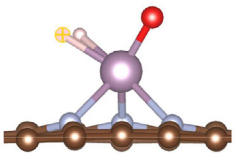 H_2 over O-Mo/N_3-Gt	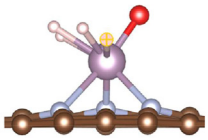 2×H_2 over O-Mo/N_3-Gt	
Binding Energy	-2.58 eV	-2.44 eV	
Electron (involved)	1.05/1.08	1.04/1.01/1.03/1.02	
Structure entry 3	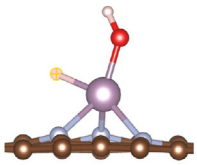 H over OH-Mo /N_3-Gt	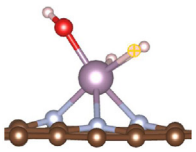 3×H over OH-Mo /N_3-Gt	
Binding Energy	-2.28 eV	-2.64 (-2.67/-2.27) eV	
Electron (involved)	1.34	1.09/1.03/1.29	

(b)

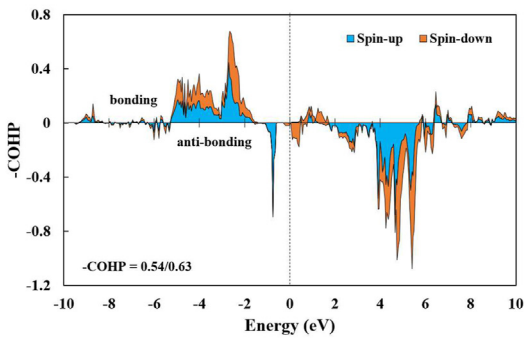

(c)

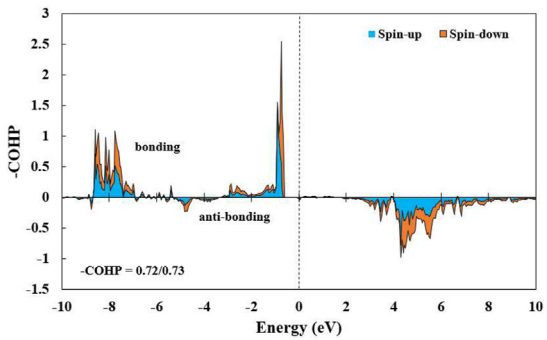

Fig. 6 – The active site of Mo_1/N_3Gt in dynamic coordination environments (a) The COHP population analysis for H–OH–Mo_1/N_3-Gt and (b) for 3H–OH–Mo_1/N_3-Gt (c).

Please cite this article as: Zhang J et al., Unveiling the mechanism of controllable CO_2 hydrogenation by group VIB metal single atom anchored on N-doped graphite: A density functional theory study, International Journal of Hydrogen Energy, https://doi.org/10.1016/j.ijhydene.2022.09.170

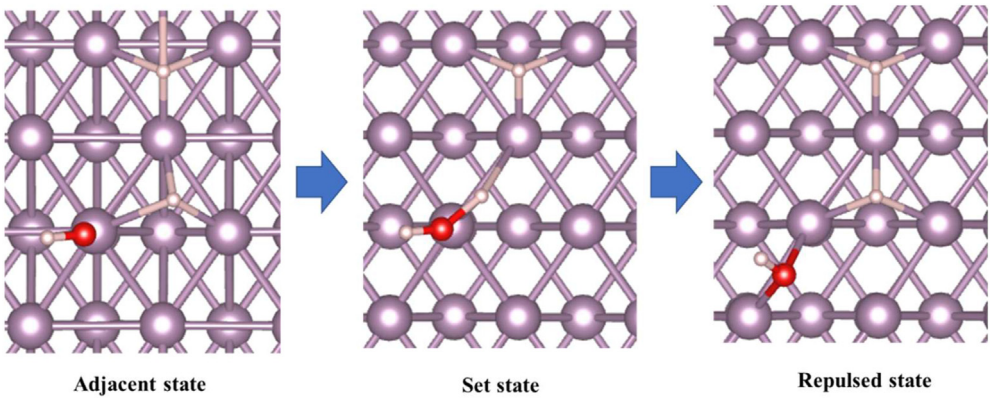

Fig. 7 – Hypothetical electrophilic attack of H* over Mo (1 1 0).

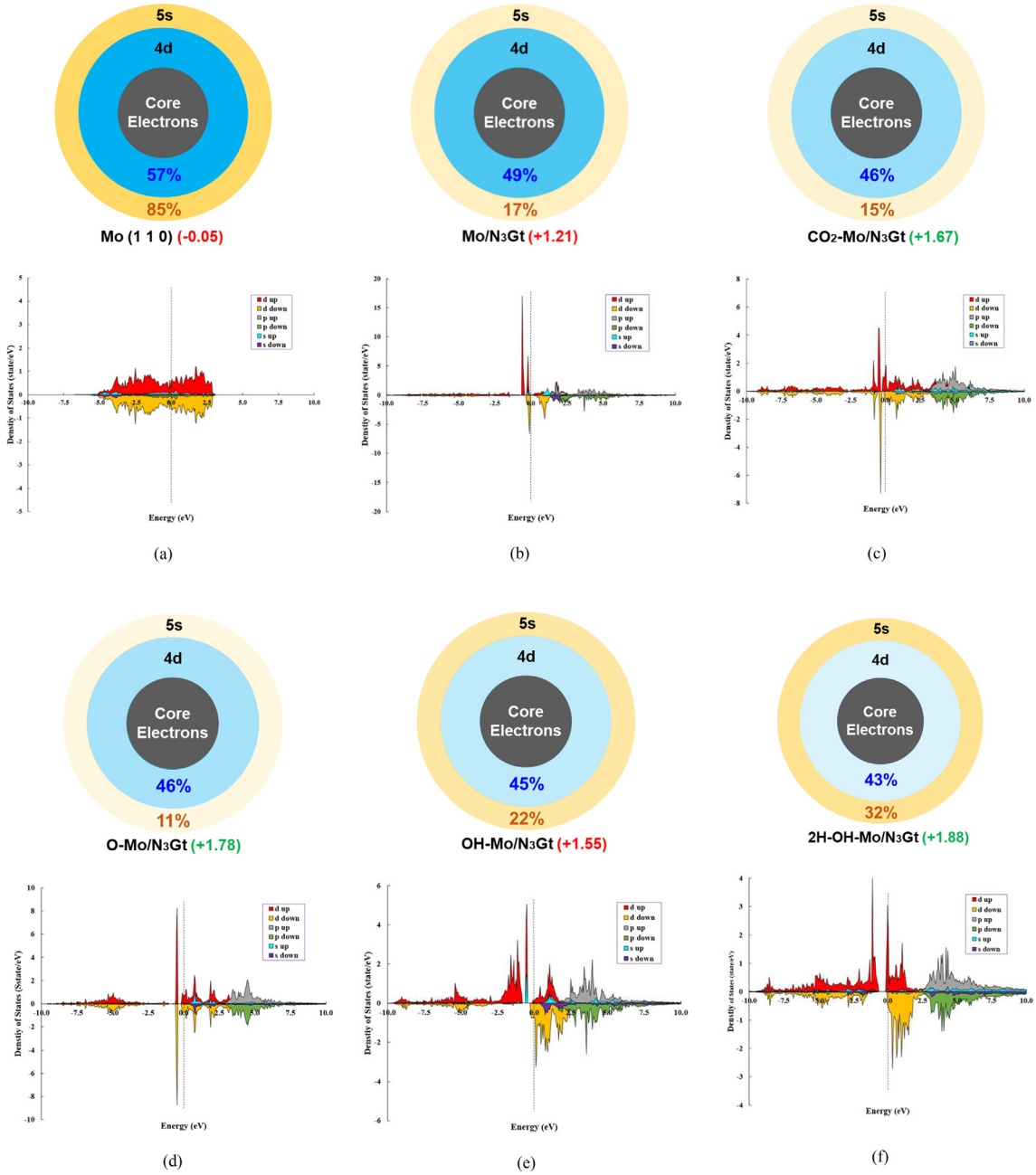

Fig. 8 – The states occupancies of 4d and 5s obits for Mo in dynamic coordination.

Please cite this article as: Zhang J et al., Unveiling the mechanism of controllable CO_2 hydrogenation by group VIB metal single atom anchored on N-doped graphite: A density functional theory study, International Journal of Hydrogen Energy, https://doi.org/10.1016/j.ijhydene.2022.09.170

unsaturable coordinated Mo in Mo (1 1 0). The occupancy for 5s is 85% and 57% for 4d orbit, and the Mo is almost electric-neutral with merely −0.05e negative charge, the metallicity of Mo leading to the surface H* being significantly negatively charged. In contrast, when Mo is coordinated in Mo_1/N_3-Gt (Fig. 8 (b)), the occupancy of 5s declines sharply to 17%, and the occupancy for 4d orbit decreases to 49%, resulting from the aforementioned electron-absorbing feature of the pyridinic nitrogen coordination, and the Mo is spotted to be more likely a cation carrying +1.21e positive charge, on which, the adsorbed H_2 was dissociated and still carried a negative charge of −0.36e/-0.25e, although this charge is much less than that over the Mo slab. The additional CO_2 adsorption onto Mo_1/N_3-Gt causes more electron lose to 4d and 5s orbits of Mo (Fig. 8 (c)), and if the active site of Mo_1/N_3-Gt is coordinated by a more electronegative species, for example O, we found the occupancy of 5s is only 11% and that for 4d is 46%, and the Mo cation carries more positive charge of +1.78e. In such a coordination environment, as aforementioned, the subsequent adsorbed H_2 would be able to avoid getting much negatively charged and remain almost electric neutral, giving rise to much more facile production of *OH over Mo_1/N_3-Gt. In the scenario that Mo_1/N_3-Gt is coordinated with a sole *OH, the occupancy of 5s orbit is 22% and that for 4d is 45%, and the charge on Mo cation is +1.55e (Fig. 7 (e)), which is not enough to catalyze hydrogenation, as shown in Fig. 5 (c) and (d). However, with the additional coordination of H_2 on *OH−Mo_1/N_3-Gt, we found the occupancy of 4d experiences a further decrease to 43%. Meanwhile, the occupancy of 5s increases to 32%, indicating an electron lose from 4d orbit and an electron enrichment to 5s. As a result, the charge of Mo cation increased to +1.88e, which could eventually give rise to the nearly neutral H* and benefit the H_2O formation over Mo_1/N_3-Gt. Besides, the decreasing d-state occupancy has also been reported to facilitate the CO_2 activation through the redox pathway [57].

The modelling results so far have revealed that the electron structures of the central Mo directly determine the charge of H*, which has fundamental links to its migration feature and the subsequent hydrogenation behavior. $Mo^{\delta+}$ gives rise to the surface H* neutrality when it carries no less than +1.7e of positive charge. The dynamic coordination of the electron deficient groups, including CO_2* and O* over the Mo_1/N_3-Gt during reaction, is found to be beneficial for tuning the charge of H* by lowering the occupancies of 5s and 4d orbits of the central Mo atom, thus facilitating the hydrogenation process. The additional H_2 adsorption would also be able to give rise to the less negative charge of H* by cutting down the occupancy in the 4d orbit of Mo, in line with the reaction modelling result that additional H_2 adsorption would lead to more ready H_2O formation. This is also in agreement with the observation in the H_2O formation over Cr_1/N_3-Gt, where the co-adsorption of CO* with both *OH and H* would much facilitate the H_2O formation via decreasing the energy barrier by 0.8 eV.

Conclusions

The present research provided comprehensive reactive analyses of CO_2 hydrogenation to CO over the graphite supported metal-based SACs. Group VIB metal-based catalysts outperformed other 15 metal candidates through effective electron injection to CO_2 and lowering escaping energy of the products, and the SACs had superior activation effects of CO_2 compared to the single atom in a corresponding metal facet. Reaction pathway modelling revealed Mo_1/N_3-Gt and W_1/N_3-Gt were effective for spontaneous decomposition of CO_2 and H_2, and Mo_1/N_3-Gt gave rise to special barrier-free production of CO during the dissociative adsorption and lowered the peak energy barrier for the hydrogenation of the surface O* species to 1.10 eV H_2O formation was observed to be the potential rate-controlling step for CO_2 hydrogenation over all the SACs, wherein direct hydrogenation could hardly take place but turned out to be facile with the additional adsorbed H_2. H migration capacity was considered to affect such selective hydrogenation reaction. In contrast to the bond strength of both H*-Mo and O*-Mo, charge on H* was found to be the determining factor affecting the H migration and the H_2O formation reaction. The electron negativity of Mo cation was observed to be a potential descriptor that was affecting the hydrogen charge and subsequent hydrogenation, and it changed with the dynamic coordination during the reaction. The electron deficient groups (ligand) such as O*and CO_2* were important to diluting the occupancies for 4d or 5s obit of the $Mo^{\delta+}$ in order to benefit hydrogenation. Additional H_2 adsorption may also give rise to a lower 4d-occupancy although it slightly promoted the occupancy of 5s. The hydrogenation and H_2O formation became more ready given the lower electron occupancy of central Mo atom of Mo_1/N_3-Gt, and the optimal positive charge of $Mo^{\delta+}$ for a neutral hydrogen and facile hydrogenation was found to be no less than +1.7e based on the Bader's analysis system.

Author contributions

J.Z.: Conceptualization, Methodology, Investigation, Writing - Original Draft & Editing, Funding acquisition and Project management. **B.Y.**: Supervision, Funding acquisition and Writing - Review & Editing. **K.H.L.**: Research supervision, Writing - Review & Editing, and Provision of supercomputing resources.

Declaration of competing interest

The authors declare that they have no known competing financial interests or personal relationships that could have appeared to influence the work reported in this paper.

Acknowledgements

The authors acknowledge the financial support from the National Natural Science Foundation of China (NSFC, Grant No. 52206156), Fellowship of China Postdoctoral Science Foundation (2021M701851) and "Shuimu Scholar" scheme at Tsinghua University (2019SM127). The work is also supported by the Seed Fund of Shanxi Research Institute for Clean Energy, Tsinghua University. Support from the UK Engineering and

Please cite this article as: Zhang J et al., Unveiling the mechanism of controllable CO_2 hydrogenation by group VIB metal single atom anchored on N-doped graphite: A density functional theory study, International Journal of Hydrogen Energy, https://doi.org/10.1016/j.ijhydene.2022.09.170

Physical Sciences Research Council under the project "UK Consortium on Mesoscale Engineering Sciences (UKCOMES)" (Grant No. EP/R029598/1) is gratefully acknowledged. This work made use of computational support by CoSeC, the Computational Science Centre for Research Communities, through UKCOMES.

Appendix A. Supplementary data

Supplementary data to this article can be found online at https://doi.org/10.1016/j.ijhydene.2022.09.170.

REFERENCES

[1] IEA. Net. Zero by 2050: a roadmap for the global energy sector. International Energy Agency; 2021. p. 224.
[2] Artz J, Müller TE, Thenert K, Kleinekorte J, Meys R, Sternberg A, et al. Sustainable conversion of carbon dioxide: an integrated review of catalysis and life cycle assessment. Chem Rev 2018;118:434–504. https://doi.org/10.1021/acs.chemrev.7b00435.
[3] Porosoff MD, Yan B, Chen JG. Catalytic reduction of CO2 by H2 for synthesis of CO, methanol and hydrocarbons: challenges and opportunities. Energy Environ Sci 2016;9:62–73. https://doi.org/10.1039/C5EE02657A.
[4] Gao P, Li S, Bu X, Dang S, Liu Z, Wang H, et al. Direct conversion of CO2 into liquid fuels with high selectivity over a bifunctional catalyst. Nat Chem 2017;9:1019–24. https://doi.org/10.1038/nchem.2794.
[5] Wei J, Ge Q, Yao R, Wen Z, Fang C, Guo L, et al. Directly converting CO2 into a gasoline fuel. Nat Commun 2017;8:1–8. https://doi.org/10.1038/ncomms15174.
[6] Zhang Q, Pastor-Pérez L, Wang Q, Ramirez Reina T. Conversion of CO2 to added value products via rWGS using Fe-promoted catalysts: carbide, metallic Fe or a mixture? J Energy Chem 2022;66:635–46. https://doi.org/10.1016/j.jechem.2021.09.015.
[7] Pastor-Pérez L, Baibars F, Le Sache E, Arellano-García H, Gu S, Reina TR. CO2 valorisation via reverse water-gas shift reaction using advanced Cs doped Fe-Cu/Al2O3 catalysts. J CO2 Util 2017;21:423–8. https://doi.org/10.1016/j.jcou.2017.08.009.
[8] Zhou G, Xie F, Deng L, Zhang G, Xie H. Supported mesoporous Cu/CeO2-δ catalyst for CO2 reverse water–gas shift reaction to syngas. Int J Hydrogen Energy 2020;45:11380–93. https://doi.org/10.1016/j.ijhydene.2020.02.058.
[[9]] Malik AS, Bali H, Czirok F, Szamosvölgyi Á, Halasi G, Efremova A, et al. Turning CO2 to CH4 and CO over CeO2 and MCF-17 supported Pt, Ru and Rh nanoclusters – influence of nanostructure morphology, supporting materials and operating conditions. Fuel 2022;326:124994. https://doi.org/10.1016/j.fuel.2022.124994.
[10] Zhao X, Wu Z, Fu J, Guo J, Kang S. Designing FeO@graphite@C Nanocomposites based on Humins as efficient catalysts for reverse water-gas shift. ACS Appl Mater Interfaces 2021;13:57100–6. https://doi.org/10.1021/acsami.1c15791.
[11] Ebrahimi P, Kumar A, Khraisheh M. Combustion synthesis of copper ceria solid solution for CO2 conversion to CO via reverse water gas shift reaction. Int J Hydrogen Energy 2022. https://doi.org/10.1016/j.ijhydene.2021.12.142.
[12] Ai X, Xie H, Chen S, Zhang G, Xu B, Zhou G. Highly dispersed mesoporous Cu/γ-Al2O3 catalyst for RWGS reaction. Int J Hydrogen Energy 2022;47:14884–95. https://doi.org/10.1016/j.ijhydene.2022.03.002.
[13] Kattel S, Yan B, Yang Y, Chen JG, Liu P. Optimizing binding energies of key intermediates for CO 2 hydrogenation to methanol over oxide-supported copper. J Am Chem Soc 2016;138:12440–50. https://doi.org/10.1021/jacs.6b05791.
[14] Fujita S. Mechanism of the reverse water gas shift reaction over Cu/ZnO catalyst*1. J Catal 1992;134:220–5. https://doi.org/10.1016/0021-9517(92)90223-5.
[15] Liu Y, Murthy PR, Zhang X, Wang H, Shi C. Phase transformation of iron oxide to carbide and Fe 3 C as an active center for the RWGS reaction. New J Chem 2021;45:22444–9. https://doi.org/10.1039/D1NJ04120G.
[16] Marquart W, Raseale S, Prieto G, Zimina A, Sarma BB, Grunwaldt J-D, et al. CO 2 reduction over Mo 2 C-based catalysts. ACS Catal 2021;11:1624–39. https://doi.org/10.1021/acscatal.0c05019.
[17] Peng L, Jurca B, Primo A, Gordillo A, Parvulescu VI, García H. Co–Fe clusters supported on N-doped graphitic carbon as highly selective catalysts for reverse water gas shift reaction. ACS Sustainable Chem Eng 2021;9:9264–72. https://doi.org/10.1021/acssuschemeng.1c01401.
[18] Zhang Q, Pastor-pérez L, Zhang X, Gu S, Reina TR. CO 2 conversion to value-added gas-Phase products. In: Tomas RR, Odriozola AJ, Arellano-Garcia H, editors. Engineering solutions for CO2 conversion. 1st ed. 2021.
[19] Wang L-X, Guan E, Wang Z, Wang L, Gong Z, Cui Y, et al. Dispersed Nickel Boosts catalysis by copper in CO 2 hydrogenation. ACS Catal 2020;10:9261–70. https://doi.org/10.1021/acscatal.0c00907.
[20] Santos J, Bobadilla L, Centeno M, Odriozola J. Operando DRIFTS-MS study of WGS and rWGS reaction on biochar-based Pt catalysts: the promotional effect of Na. Journal of Carbon Research 2018;4:47. https://doi.org/10.3390/c4030047.
[21] Zhang X, Han S, Zhu B, Zhang G, Li X, Gao Y, et al. Reversible loss of core–shell structure for Ni–Au bimetallic nanoparticles during CO2 hydrogenation. Nature Catalysis 2020;3:411–7. https://doi.org/10.1038/s41929-020-0440-2.
[22] Ou Z, Qin C, Niu J, Zhang L, Ran J. A comprehensive DFT study of CO2 catalytic conversion by H2 over Pt-doped Ni catalysts. Int J Hydrogen Energy 2019;44:819–34. https://doi.org/10.1016/j.ijhydene.2018.11.008.
[23] Porosoff MD, Yang X, Boscoboinik JA, Chen JG. Molybdenum carbide as alternative catalysts to precious metals for highly selective reduction of CO2 to CO. Angew Chem Int Ed 2014;53:6705–9. https://doi.org/10.1002/anie.201404109.
[24] Lim HS, Lee M, Kim Y, Kang D, Lee JW. Low-temperature CO2 hydrogenation to CO on Ni-incorporated LaCoO3 perovskite catalysts. Int J Hydrogen Energy 2021;46:15497–506. https://doi.org/10.1016/j.ijhydene.2021.02.085.
[25] Bobadilla LF, Santos JL, Ivanova S, Odriozola JA, Urakawa A. Unravelling the role of oxygen vacancies in the mechanism of the reverse water-gas shift reaction by operando DRIFTS and ultraviolet-visible spectroscopy. ACS Catal 2018;8:7455–67. https://doi.org/10.1021/acscatal.8b02121.
[26] Bobadilla LF, Santos JL, Ivanova S, Odriozola JA, Urakawa A. Unravelling the role of oxygen vacancies in the mechanism of the reverse water–gas shift reaction by operando DRIFTS and ultraviolet–visible spectroscopy. ACS Catal 2018;8:7455–67. https://doi.org/10.1021/acscatal.8b02121.
[27] Maneerung T, Hidajat K, Kawi S. K-doped LaNiO3 perovskite for high-temperature water-gas shift of reformate gas: role of potassium on suppressing methanation. Int J Hydrogen Energy 2017;42:9840–57. https://doi.org/10.1016/j.ijhydene.2017.01.060.
[28] Kumari N, Haider MA, Agarwal M, Sinha N, Basu S. Role of reduced CeO 2 (110) surface for CO 2 reduction to CO and methanol. J Phys Chem C 2016;120:16626–35. https://doi.org/10.1021/acs.jpcc.6b02860.

Please cite this article as: Zhang J et al., Unveiling the mechanism of controllable CO_2 hydrogenation by group VIB metal single atom anchored on N-doped graphite: A density functional theory study, International Journal of Hydrogen Energy, https://doi.org/10.1016/j.ijhydene.2022.09.170

[29] Cui T, Li L, Ye C, Li X, Liu C, Zhu S, et al. Heterogeneous single atom environmental catalysis: Fundamentals, applications, and opportunities. Adv Funct Mater 2021:2108381. https://doi.org/10.1002/adfm.202108381. 2108381.
[30] Zhao Z, Wang M, Ma P, Zheng Y, Chen J, Li H, et al. Atomically dispersed Pt/CeO2 catalyst with superior CO selectivity in reverse water gas shift reaction. Appl Catal B Environ 2021;291:120101. https://doi.org/10.1016/j.apcatb.2021.120101.
[31] Rodriguez JA, Evans J, Feria L, Vidal AB, Liu P, Nakamura K, et al. CO2 hydrogenation on Au/TiC, Cu/TiC, and Ni/TiC catalysts: production of CO, methanol, and methane. J Catal 2013;307:162–9. https://doi.org/10.1016/j.jcat.2013.07.023.
[32] Wang A, Li J, Zhang T. Heterogeneous single-atom catalysis. Nat Rev Chem 2018;2:65–81. https://doi.org/10.1038/s41570-018-0010-1.
[33] Kwak JH, Kovarik L, Szanyi J. Heterogeneous catalysis on atomically dispersed supported metals: CO 2 reduction on multifunctional Pd catalysts. ACS Catal 2013;3:2094–100. https://doi.org/10.1021/cs4001392.
[34] Zhu J, Cannizzaro F, Liu L, Zhang H, Kosinov N, Filot IAW, et al. Ni–In Synergy in CO 2 hydrogenation to methanol. ACS Catal 2021;11:11371–84. https://doi.org/10.1021/acscatal.1c03170.
[35] Shao X, Yang X, Xu J, Liu S, Miao S, Liu X, et al. Iridium single-atom catalyst performing a quasi-homogeneous hydrogenation transformation of CO2 to formate. Chem 2019;5:693–705. https://doi.org/10.1016/j.chempr.2018.12.014.
[36] Ye X, Yang C, Pan X, Ma J, Zhang Y, Ren Y, et al. Highly selective hydrogenation of CO2to ethanol via designed bifunctional Ir1-In2O3Single-atom catalyst. J Am Chem Soc 2020;142:19001. https://doi.org/10.1021/jacs.0c08607. 5.
[37] Su X, Yang X-F, Huang Y, Liu B, Zhang T. Single-atom catalysis toward efficient CO 2 conversion to CO and formate products. Accounts Chem Res 2019;52:656–64. https://doi.org/10.1021/acs.accounts.8b00478.
[38] Wang Y, Arandiyan H, Scott J, Aguey-Zinsou K-F, Amal R. Single atom and Nanoclustered Pt catalysts for selective CO 2 reduction. ACS Appl Energy Mater 2018;1:6781–9. https://doi.org/10.1021/acsaem.8b00817.
[39] Millet M-M, Algara-Siller G, Wrabetz S, Mazheika A, Girgsdies F, Teschner D, et al. Ni single atom catalysts for CO 2 activation. J Am Chem Soc 2019;141:2451–61. https://doi.org/10.1021/jacs.8b11729.
[40] Chen X, Su X, Su HY, Liu X, Miao S, Zhao Y, et al. Theoretical insights and the corresponding Construction of supported metal catalysts for highly selective CO2 to CO conversion. ACS Catal 2017;7:4613–20. https://doi.org/10.1021/acscatal.7b00903.
[41] Bu S, Yao N, Hunter MA, Searles DJ, Yuan Q. Design of two-dimensional carbon-nitride structures by tuning the nitrogen concentration. Npj Computational Materials 2020;6. https://doi.org/10.1038/s41524-020-00393-5.
[42] Witoon T, Numpilai T, Nueangnoraj K, Cheng CK, Chareonpanich M, Limtrakul J. Light olefins synthesis from CO2 hydrogenation over mixed Fe–Co–K supported on micro-mesoporous carbon catalysts. Int J Hydrogen Energy 2021. https://doi.org/10.1016/j.ijhydene.2021.10.265.
[43] Gong L, Zhang D, Lin C, Zhu Y, Shen Y, Zhang J, et al. Catalytic mechanisms and design principles for single-atom catalysts in highly efficient CO 2 conversion. Adv Energy Mater 2019;9:1902625. https://doi.org/10.1002/aenm.201902625.
[44] Gu J, Hsu CS, Bai L, Chen HM, Hu X. Atomically dispersed Fe3+ sites catalyze efficient CO2 electroreduction to CO. Science 2019;364:1091–4. https://doi.org/10.1126/science.aaw7515.
[45] Dhabarde N, Selvaraj J, Yuda A, Kumar A, Subramanian VR. Review of photocatalytic and photo-electrocatalytic reduction of CO2 on carbon supported films. Int J Hydrogen Energy 2022. https://doi.org/10.1016/j.ijhydene.2022.02.124.
[46] Koshy DM, Nathan SS, Asundi AS, Abdellah AM, Dull SM, Cullen DA, et al. Bridging thermal catalysis and Electrocatalysis: Catalyzing CO 2 conversion with carbon-based materials. Angew Chem Int Ed 2021;60:17472–80. https://doi.org/10.1002/anie.202101326.
[47] Esrafili MD, Nejadebrahimi B. Theoretical insights into hydrogenation of CO 2 to formic acid over a single Co atom incorporated nitrogen-doped graphene: a DFT study. Appl Surf Sci 2019;475:363–71. https://doi.org/10.1016/j.apsusc.2018.12.302.
[48] Sredojević DN, Šljivančanin Ž, Brothers EN, Belić MR. Formic acid synthesis by CO 2 hydrogenation over single-atom catalysts based on Ru and Cu Embedded in graphene. ChemistrySelect 2018;3:2631–7. https://doi.org/10.1002/slct.201702836.
[49] Ma J, Gong H, Zhang T, Yu H, Zhang R, Liu Z, et al. Hydrogenation of CO2 to formic acid on the single atom catalysis Cu/C2N: a first principles study. Appl Surf Sci 2019;488:1–9. https://doi.org/10.1016/j.apsusc.2019.03.187.
[50] Ali S, Iqbal R, Khan A, Rehman SU, Haneef M, Yin L. Stability and catalytic performance of single-atom catalysts supported on doped and Defective graphene for CO2Hydrogenation to formic acid: a first-principles study. ACS Appl Nano Mater 2021;4:6893–902. https://doi.org/10.1021/acsanm.1c00959.
[51] Perdew JP, Burke K, Ernzerhof M. Generalized gradient approximation made Simple. Phys Rev Lett 1996;77:3865–8. https://doi.org/10.1103/PhysRevLett.77.3865.
[52] Grimme S. Semiempirical GGA-type density functional constructed with a long-range dispersion correction. J Comput Chem 2006;27:1787–99. https://doi.org/10.1002/jcc.20495.
[53] Lejaeghere K, Van Speybroeck V, Van Oost G, Cottenier S. Error Estimates for solid-state density-functional theory predictions: an Overview by Means of the Ground-state elemental crystals. Crit Rev Solid State Mater Sci 2014;39:1–24. https://doi.org/10.1080/10408436.2013.772503.
[54] Pickard CJ, Winkler B, Chen RK, Payne MC, Lee MH, Lin JS, et al. Structural Properties of Lanthanide and Actinide compounds within the plane wave pseudopotential Approach. Phys Rev Lett 2000;85:5122–5. https://doi.org/10.1103/PhysRevLett.85.5122.
[55] Natta G, Passerini L. Solid solutions, isomorphism and symmetry between the oxides of bivalent metals. - 1. Systems: CaO-CdO, CaO-MnO, CaO-CoO, CaO-NiO, CaO-MgO. Gazz Chim Ital 1929;59:129–54.
[56] Graciani J, Mudiyanselage K, Xu F, Baber AE, Evans J, Senanayake SD, et al. Highly active copper-ceria and copper-ceria-titania catalysts for methanol synthesis from CO 2. Science 2014;345:546–50. https://doi.org/10.1126/science.1253057.
[57] Ocampo-Restrepo VK, Verga LG, Da Silva JLF. Ab initio study of the C–O bond dissociation in CO 2 reduction by redox and carboxyl Routes on 3d transition metal systems. J Phys Chem C 2021;125:26296–306. https://doi.org/10.1021/acs.jpcc.1c05468.
[58] Figueras M, Gutiérrez RA, Viñes F, Ramírez PJ, Rodriguez JA, Illas F. Supported Molybdenum carbide nanoparticles as an Excellent catalyst for CO 2 hydrogenation. ACS Catal 2021;11:9679–87. https://doi.org/10.1021/acscatal.1c01738.
[59] Doherty F, Goldsmith BR. Rhodium single-atom catalysts on titania for reverse water gas shift reaction Explored by first principles Mechanistic analysis and compared to nanoclusters. ChemCatChem 2021;13:3155–64. https://doi.org/10.1002/cctc.202100292.
[60] Pozzo M, Alfè D. Hydrogen dissociation and diffusion on transition metal (=Ti, Zr, V, Fe, Ru, Co, Rh, Ni, Pd, Cu, Ag)-doped Mg(0001) surfaces. Int J Hydrogen Energy 2009;34:1922–30. https://doi.org/10.1016/j.ijhydene.2008.11.109.

Please cite this article as: Zhang J et al., Unveiling the mechanism of controllable CO_2 hydrogenation by group VIB metal single atom anchored on N-doped graphite: A density functional theory study, International Journal of Hydrogen Energy, https://doi.org/10.1016/j.ijhydene.2022.09.170